Check for updates

Enhancement of CO gas sensing performance by Mn-doped porous ZnSnO₃ microspheres†

Manish Kumar Tiwari, [ID] [a] Subhash Chand Yadav, [ID] [a] Abhishek Srivastava,[a] Archana Kanwade, [ID] [a] Jena Akash Kumar Satrughna, [ID] [b] Sawanta S. Mali, [ID] [c] Jyoti V. Patil,[c] Chang Kook Hong[c] and Parasharam M. Shirage [ID] *[a]

This work reports the synthesis of Mn-doped ZnSnO₃ microspheres ($Zn_{1-x}Mn_xSnO_3$) using a simple co-precipitation method with ($x = 0$ to 0.15) and characterized for structural, morphological, surface area, and sensing properties. X-ray diffraction (XRD) analysis revealed the face-centered cubic structure of Mn-doped ZnSnO₃ samples. Brunauer–Emmett–Teller (BET) analysis demonstrated the variation in surface area from 15.229 m² g⁻¹ to 42.999 m² g⁻¹ with $x = 0$ to 0.15 in $Zn_{1-x}Mn_xSnO_3$. XPS indicates the change in the defect levels by Mn doping, which plays a crucial role in chemical sensors. Indeed a significant increase ($\approx 311.37\%$) in CO gas sensing response was observed in the $x = 0.10$ sample compared to pure ZnSnO₃ with a simultaneous reduction in operating temperature from 250 to 200 °C. Moreover, remarkable enhancements in response/recovery times ($\approx 6.6/34.1$ s) were obtained in the $x = 0.10$ sample. The Mn-doped ZnSnO₃ could be a promising candidate for CO gas sensing devices used for maintaining air quality.

1 Introduction

Rapid industrialization and urbanization adversely affect the environment and human health, resulting in acid rain, ozone depletion, downgraded air quality, global warming, and the emission of various harmful gases.[1] Among different hazardous gases, carbon monoxide (CO) is the most critical air pollutant, which is generated from the incomplete combustion process of fossil fuels, wood, charcoal, petroleum products, and the burnout of electrical appliances.[2] The detection of CO is equally tricky owing to its colorless and odorless properties.[3] It can cause death by forming carboxyhemoglobin by mixing with blood during breathing.[4] Note that the exposure limit for CO is 50 ppm; hence precise monitoring is essential to reduce disastrous effects.

Metal oxide semiconductor (MOS) based gas sensors of chemiresistive-type have been extensively studied for detecting various harmful gases owing to their diversified features such as excellent sensitivity, fast response, low maintenance cost, and suitability for portable instruments.[5] The working principle of MOS is based on the change in resistance of the sensing material. However, the high operating temperature and imperfect selectivity limit their practical applications. In this regard, ternary ABO₃ perovskite[6,7] structured MOS sensors have attracted the scientific community over the binary MOS sensors due to the presence of multiple cation sites for doping materials and exhibiting more potential for enhancing the device performance in gas sensing applications. Out of various choices, the zinc stannate (ZnSnO₃) ternary compound (n-type MOS) is a potential candidate due to its high electron mobility, conductivity, good stability, and attractive physical and chemical properties[8] compared to binary counterparts ZnO and SnO₂. These properties enable this material to be employed in various applications such as Li-ion batteries,[9] solar cells,[10] photocatalysts,[11] gas sensing, *etc.*[12]

Several studies have been reported on gas sensing properties of porous ZnSnO₃ material, especially on volatile organic compounds (VOCs) such as acetone,[13] ethanol,[14] butanol,[15] propanol,[16] formaldehyde,[17] and triethylamine.[18] However, very few studies are available on the detection of gases except H₂S[12] and H₂.[19] Pure ZnSnO₃ material usually suffers a requirement barrier due to low sensitivity, poor selectivity, and high operating temperature for the detection of gases other than VOCs. It is known that doping ternary MOS materials with transition metals can significantly enhance the gas sensing performance as it can change the interaction between the gases, oxygen molecules, and the surface electron due to an increase in porosity and large specific surface areas. Despite this, the available studies to improve the gas sensing properties on

[a]Department of Metallurgy Engineering and Materials Science, Indian Institute of Technology Indore, Simrol, Khandwa Road, Indore 453552, India. E-mail: pmshirage@iiti.ac.in; paras.shirage@gmail.com

[b]Department of Physics, Indian Institute of Technology Indore, Simrol, Khandwa Road, Indore 453552, India

[c]Polymer Energy Materials Laboratory, School of Chemical Engineering, Chonnam National University, Gwangju 61186, South Korea

† Electronic supplementary information (ESI) available. See DOI: https://doi.org/10.1039/d2ra06785d

$ZnSnO_3$ doped with transition metals are significantly fewer. For instance, Fe,[20] Al,[21] Mg,[22] and Pd[23] have been doped in $ZnSnO_3$ for performance improvement.

I. Karaduman *et al.*[24] and E. Della Gaspera *et al.*[25] have reported the doping of transition metal Mn to ZnO compounds where improvement of CO sensing was ascribed to the multiple oxidation states of Mn, preferred adsorption of CO molecules at the transition metal dopant sites and then their migration from Mn or Cu sites to Zn sites, and large specific surface area with increased oxygen adsorption and its reactivity with CO molecules.

In correspondence to the above discussion, we decided to figure out the sensing capabilities of $ZnSnO_3$ doped with different concentrations of Mn. This article presents a simple and economical technique for the synthesis of $ZnSnO_3$ with different loadings of Mn ($Zn_{1-x}Mn_xSnO_3$, $x = 0$ to 0.15) using co-precipitation method and systematic investigation of structural and morphological properties. Then, the prepared material was used to fabricate the gas sensor device based on the resistance change model. The sensing material was exposed to different interfering gases such as ammonia, carbon dioxide, ethanol, and CO to test the selective sensing properties. Among these, CO turned out to be highly selectively sensed by ($Zn_{1-x}Mn_xSnO_3$, $x = 0$ to 0.15). Being highly sensitive to CO among these gases, sensing measurements of Mn-doped $ZnSnO_3$ samples were achieved for different concentrations of CO. The best-performing device was subjected to long-term stability and reproducibility tests for repeated cycles. Finally, the plausible gas-sensing mechanism is discussed to postulate the influence of Mn doping in the $ZnSnO_3$ perovskite microstructure.

2 Experimental section

2.1 Materials

Zinc sulfate heptahydrate ($ZnSO_4 \cdot 7H_2O$, >99.5%), sodium stannate trihydrate ($Na_2SnO_3 \cdot 3H_2O$, >99%), manganese sulfate monohydrate ($MnSO_4 \cdot H_2O$, >99%), and ammonia solution (NH_3, ~25%) were of analytical grade and purchased from Sigma-Aldrich Co. Ltd. All the reagents were used without any further purification.

2.2 Synthesis of pure and Mn-doped $ZnSnO_3$ microspheres

Pure and Mn-doped $ZnSnO_3$ microspheres were synthesized by a simple co-precipitation method. In a typical experiment, 0.1 M of zinc sulfate heptahydrate was dissolved in 50 mL of deionized water. The solution was strenuously stirred at room temperature until the clear transparent solution was accomplished. Likewise, 0.1 M of sodium stannate trihydrate was added to 50 mL of deionized water and stirred. Then, under perpetual stirring, appropriate aqueous ammonia solution was poured dropwise continuously into the $ZnSO_4$ solution to maintain a pH ~ 10. In the next step, a certain amount of $MnSO_4 \cdot H_2O$ was dissolved in the above $ZnSO_4$ solution. Then, the sodium stannate solution was added to the above solution ([Zn]/[Sn] = 1 : 1), and the aftermath mixed solution was stirred strenuously for 2 h at 60 °C. Finally, after the chemical reaction between the

precursors, the precipitates were cumulated by centrifugation at 5000 rpm and repeatedly rinsed with deionized water to remove any product contamination. Ultimately, the final products were then kept for drying in a hot oven at 100 °C for 10 h. The as-prepared pure and Mn-doped $ZnSn(OH)_6$ were subjected to heat treatment at 500 °C for 4 h in a muffle furnace to get the pure and Mn-doped $ZnSnO_3$ spherical particles. The final products with calculated Mn content 0, 2.5, 5, 7.5, 10, and 15 atomic (at)% were named as ZSO, $Z_{0.975}Mn_{0.025}SO$, $Z_{0.95}Mn_{0.05}SO$, $Z_{0.925}Mn_{0.075}SO$, $Z_{0.9}Mn_{0.1}SO$, and $Z_{0.85}Mn_{0.15}SO$, respectively.

2.3 Characterization and measurements

The crystal structure, composition, and phase of the powder samples were identified using the X-ray diffraction (XRD, Empyrean, Malvern Panalytical X-ray diffractometer) method with Cu-K$_\alpha$ radiation ($\lambda = 1.54$ Å) in the 2θ range of 10°–80°. The surface morphology of the powder samples was observed by field emission scanning electron microscopy (FESEM, JEOL, JSM-7610F plus) equipped with EDX (energy dispersive X-ray) system to perform the elemental mapping and energy-dispersive spectrum (EDS) characterization. Thermogravimetric and differential thermogravimetric analysis of the as-prepared powder samples were investigated using TGA-DSC (PerkinElmer, STA8000) at a heating rate of 5 °C min^{-1} up to 1000 °C in an N_2 atmosphere. The FTIR (Fourier transform infrared) spectra were recorded by a BRUKER TENSOR 27 spectrometer in the range of 4000–400 cm^{-1}. The specific BET surface area and porosity were figured out from N_2 adsorption–desorption measurements, which were recorded on a Quantachrome ASiQwin analyzer, taking place at ~77 K at liquid nitrogen temperature. X-ray photoelectron spectroscopy (XPS) measurements were carried out using a Kratos AXIS spectrometer with an Al K$_\alpha$ source ($hv = 1486.6$ eV).

2.4 Fabrication of the sensing device and measurements

The pure ZSO and Mn-doped ZSO samples in the powder forms were pressed into pellets of 10 mm diameter (shown in Fig. S1†) by using the hand operated hydraulic press machine under a constant load of 14 tons and then the pellet was used for CO sensing. The ohmic contacts were designed on the pellet to fabricate the sensing element equipping it with two thin parallel silver electrodes maintaining a gap of 1 mm. A home-built setup was used to conduct the gas sensing measurements. The sensors were kept in a chamber, and silver electrode contacts were connected to a Keithley Sourcemeter directly linked to a computer PC by LabVIEW™ (National Instruments) for recording the resistance signal with respect to time. The digital mass flow controllers of Dakota Instruments were used to control the flow of dry pure target gas and zero air in the required concentration. A dynamic–static flow-through technique was used to carry out the gas sensing measurement. The performance of the gas sensing device is expressed in terms of various sensing parameters. The gas sensing response (*S*%) is defined as:

$$S\ (\%) = (R_a - R_g)/R_g \times 100 \qquad (1)$$

where, R_a and R_g are the resistance values of the gas sensing materials in the presence of air and target gas atmosphere, respectively.[26] Response time (t_{res}) can be described as the time attained by a gas sensor for the maximum change in resistance when exposed to the environment of the target gas. Recovery time (t_{rec}) is the time required by a gas sensor to recover its resistance value up to 90% of its original baseline resistance value after the target gas is removed from the sensing chamber.

3   Results and discussion

3.1   Structural characterization (XRD)

The effect of the concentration of Mn doping on the crystal structure of ZSO spherical particles was analyzed by X-ray diffraction (XRD) characterization. The XRD patterns of as-prepared pure and Mn-doped $ZnSn(OH)_6$ precursor are depicted in Fig. 1a, which agrees well with the available JCPDS card no. 20-1455. The diffraction peaks in the pattern can be indexed to a pure fcc-phase $ZnSn(OH)_6$ (space group: $Pn\overline{3}$), which is in

good agreement with the Rietveld refinement, as shown in Fig. 1b. The crystallites are preferentially oriented along the x-axis, [200] direction. Lattice parameters of the pure and Mn-doped precursors were calculated by the Rietveld refinement using the Full Prof software. The obtained lattice parameters are shown in Table 1, which depicts the minor increase in lattice parameters with the increase in Mn-doping concentration. The characteristic peaks of any other phases such as ZnO, SnO_2, and

Table 1 Lattice parameters of the samples calculated by the Rietveld refinement

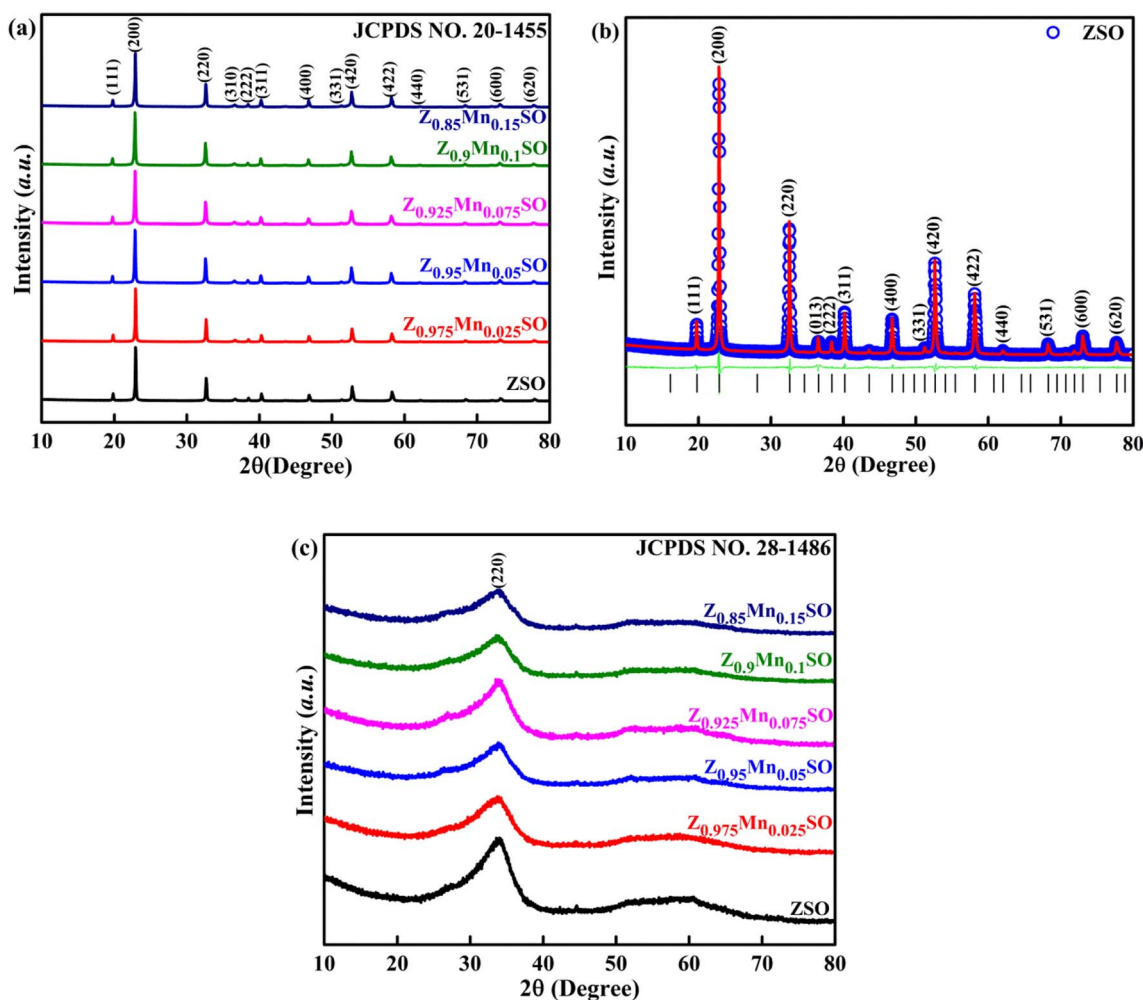| $Zn_{1-x}Mn_xSn(OH)_6$	Lattice constant (Å) $a = b = c$
$x = 0$	7.751 ± 0.004
$x = 0.025$	7.754 ± 0.002
$x = 0.05$	7.755 ± 0.001
$x = 0.075$	7.755 ± 0.006
$x = 0.1$	7.757 ± 0.003
$x = 0.15$	7.761 ± 0.003

Fig. 1   (a) XRD patterns of as-synthesized $Zn_{1-x}Mn_xSn(OH)_6$ samples (b) Rietveld refinement of the as-synthesized $ZnSn(OH)_6$ sample. (c) XRD patterns of $Zn_{1-x}Mn_xSnO_3$ samples after annealing at 500 °C.

other phases of $ZnSnO_3$ or $ZnSn(OH)_6$ were not observed, which indicates the facile substitution of Mn in $ZnSn(OH)_6$, probably due to akin ionic radius of Mn^{2+} ion (0.67 Å) with Zn^{2+} (0.74 Å).

Fig. 1c presents the XRD characterization patterns of single phase $Zn_{1-x}Mn_xSnO_3$ samples after annealing at 500 °C. Only one broad peak was observed in all diffraction peaks related to the amorphous $ZnSnO_3$ (JCPDS no. 28-1486). This indicates that all the pure and Mn-doped $ZnSn(OH)_6$ precursors were converted into the final product of the pure and Mn-doped $ZnSnO_3$ phase.

3.2 Thermal analysis (TGA-DTG)

The thermo-gravimetric analysis (TGA) was accomplished to investigate the thermal stability of as-prepared pure and Mn-doped $ZnSn(OH)_6$ samples obtained before heat treatment, and derivative TG (DTG) curves were used to examine the thermal decomposition of the samples. As shown in Fig. 2, there is a noticeable weight loss of 17.94% up to 260 °C (2.7% from 25 °C to 130 °C and 15.24% from 130 °C to 260 °C) and only about

3% weight loss is observed from 260 °C to 1000 °C (shown in Fig. S2†). Thus, the weight loss of almost 18% up to 260 °C from the precursor samples revealed the dehydration of adsorbed water from pure and Mn-doped $ZnSn(OH)_6$ samples and hence justifying the removal of hydroxyl (–OH) group to generate zinc stannate ($ZnSnO_3$) and water. Further, the weight loss of almost 3% from 260 °C to 1000 °C is accredited to the dehydration of water molecules, which were trapped within the crystals and thus required more thermal energy than the adsorbed water molecules.[27]

The DTG curves exhibit the endothermic peaks at 201.19 °C, 197.76 °C, 199.93 °C, 197.13 °C, 204.90 °C, and 197.76 °C for ZSO, $Z_{0.975}Mn_{0.025}SO$, $Z_{0.95}Mn_{0.05}SO$, $Z_{0.925}Mn_{0.075}SO$, $Z_{0.9}Mn_{0.1}SO$, and $Z_{0.85}Mn_{0.15}SO$, respectively, that could be attributed to the evaporation of residual moisture. The overall weight loss is about 21% in the whole process, which is almost very close to the earlier reported value (21%).[28] The rapid weight loss between 130 °C and 260 °C is expressed as the following chemical reaction:
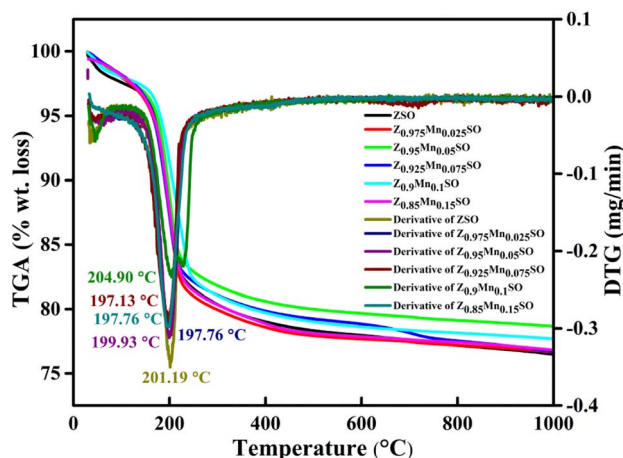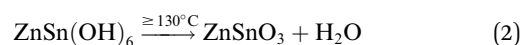
$$ZnSn(OH)_6 \xrightarrow{\geq 130°C} ZnSnO_3 + H_2O \qquad (2)$$

3.3 Fourier transform infrared (FTIR) spectrum analysis

The XRD results are also consistent with the FTIR analysis of both the as-prepared and annealed samples, Fig. 3, revealing relevant spectral changes in both cases. Fig. 3a illustrates the FTIR spectra of as-prepared pure and Mn-doped $ZnSn(OH)_6$ precursors. The broad band at ~3186 cm^{-1} is ascribed to the stretching vibration modes of –OH groups in water molecules. The other three peaks at 1169, 766, and 522 cm^{-1} are assigned to the bending and stretching vibration of M–OH or M–OH–M groups. Thus, the existence of these surface –OH groups characterizes the as-prepared samples as $ZnSn(OH)_6$. However, Fig. 3b shows the FTIR spectra of $Zn_{1-x}Mn_xSnO_3$ samples after annealing at 500 °C where all the peaks related to –OH bond vibration disappeared, indicating the dehydration of water molecules after annealing. The strong broad absorption peak at
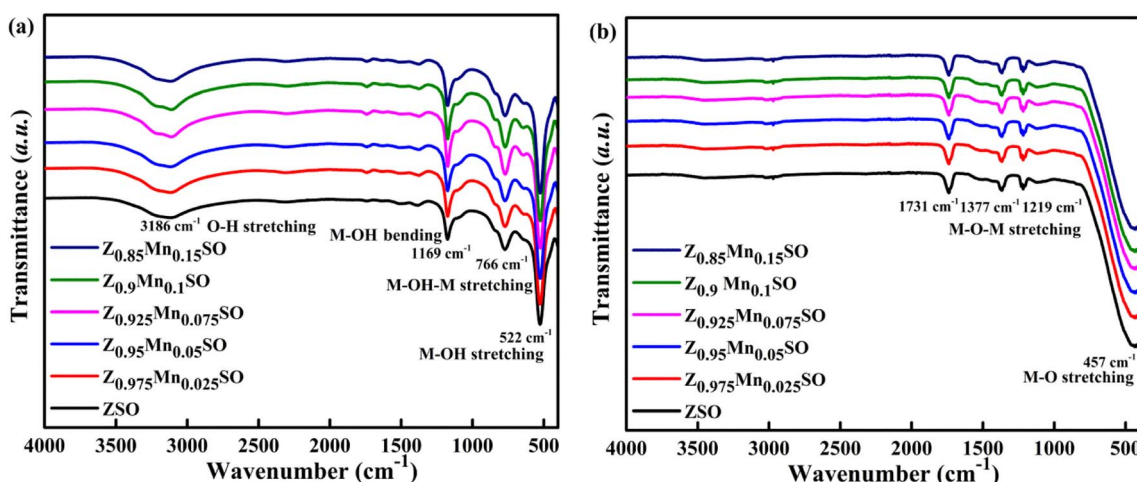

Fig. 2 TG-DTG plot of the as-prepared samples of $Zn_{1-x}Mn_xSnO_3$, $x = 0, 0.025, 0.05, 0.075, 0.1, 0.15$.

Fig. 3 FT-IR spectra of (a) as-synthesized $Zn_{1-x}Mn_xSn(OH)_6$ samples, and (b) $Zn_{1-x}Mn_xSnO_3$ samples annealed at 500 °C.

$\sim$457 cm^{-1} could be attributed to the metal oxide (M–O) bond of Zn–O and Sn–O and the small weak band observed at 1219 to 1731 cm^{-1} ascribed to the stretching vibration of M–O–M bonds[29,30] in ZnSnO$_3$. Hence, the disappearance of –OH groups during annealing and the formation of the ZnSnO$_3$ structure is clearly confirmed by the FTIR analysis.

3.4 Morphological characterization

The morphology of pure ZSO samples and with different concentrations of Mn (Zn$_{1-x}$Mn$_x$SnO$_3$, x = 0, 0.025, 0.05, 0.075, 0.1, and 0.15) after annealing at 500 °C were characterized by FE-SEM, as shown in Fig. 4. From Fig. 4a–f, it can be seen that all samples exhibit similar spherical surface morphology. It is also noted that numerous nanoparticles are stacked together to frame a porous microsphere structure. Agglomeration of particles was seen due to the high surface energy[31] of the synthesized particles. The average outer diameter of spherical particles was also calculated and found to be decreasing from 900 nm to 500 nm with an increase in the concentration of Mn. Thus, Mn doping causes an increase in surface area and creates pores in microspheres. This is conducive to the quick adsorption of target gas and reaction with the materials to give better gas sensing properties.

EDS and SEM elemental mapping were conducted to resolve the atomic ratio and specific distribution of Zn, Sn, O, and Mn elements (Z$_{0.9}$Mn$_{0.1}$SO). As shown in Fig. 5c–f, the uniform distribution of Zn, Sn, O, and Mn in the selected microsphere was clearly verified. Also, according to the EDS spectrum, Fig. 5b depicts the quantitative presence of Zn, Sn, O, and Mn elements, in addition to the Au element, which is due to the Au coating used in the analysis.

3.5 N$_2$ adsorption–desorption isotherm

N$_2$ adsorption–desorption isotherm analysis is another essential technique to elucidate the properties of gas-sensing materials in terms of parameters such as specific surface area of materials, pore-size distribution, and specific pore volume. It is well affirmed that higher gas-sensing performance is achieved for materials having higher specific surface area, and thereby, more active sites contribute to the redox reaction.[32] Fig. 6a–f represents the typical N$_2$ adsorption–desorption isotherm for the Zn$_{1-x}$Mn$_x$SnO$_3$ microspheres. Based on IUPAC classification, the resulting isotherms of these six materials can be classified as type-IV isotherms along with a defined hysteresis loop. The inset of Fig. 6a–f represents the Barrett–Joyner–Halenda (BJH) pore size distribution of all these respective six materials revealing the existence of mesoporous structures. The BET surface areas and BJH pore size diameter of all these six materials are represented in Table 2. It was observed that Mn-doped ZSO materials have a higher surface area compared to that of pure ZSO material, and the increasing trend in surface area was obtained with the increase in Mn-doping concentration. Additionally, for all these six materials, the bulk of the pores lie in the region of 3–18 nm (inset of Fig. 6a–f) and very few pores lie beyond 18 nm. The average pore diameters are 3.097, 3.088, 3.075, 3.060, 3.099, and 3.091 nm, respectively, for ZSO, Z$_{0.975}$Mn$_{0.025}$SO, Z$_{0.95}$Mn$_{0.05}$SO, Z$_{0.925}$Mn$_{0.075}$SO, Z$_{0.9}$Mn$_{0.1}$SO, and Z$_{0.85}$Mn$_{0.15}$SO. This increased surface area with a suitable mesoporous structure is advantageous to the fast adsorption of gases, promoting surface reactions, thereby remarkably enhancing the gas sensing properties of Mn-doped ZSO materials.

3.6 X-ray photoelectron spectroscopy (XPS)

Gas sensing is a surface-dominant process depending on the surface state of gas sensing materials. X-ray photoelectron spectroscopy (XPS) was used to further investigate the sensing materials for the surface elemental composition and their corresponding valence state. Fig. 7a illustrates the survey spectra of
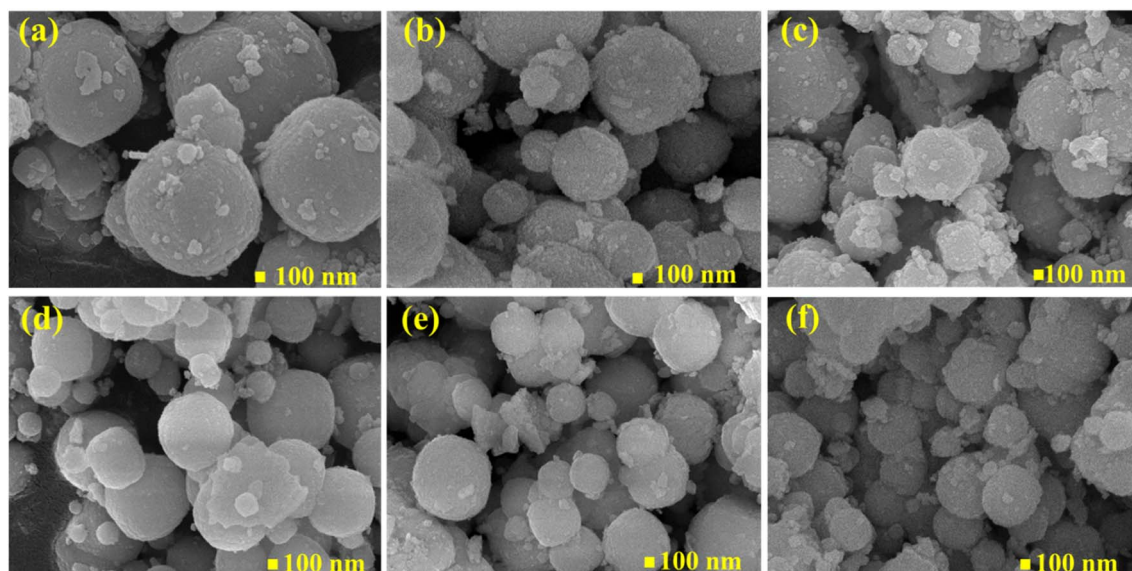

Fig. 4 FESEM images of Zn$_{1-x}$Mn$_x$SnO$_3$ spherical particles, x = (a) 0, (b) 0.025, (c) 0.05, (d) 0.075, (e) 0.1, (f) 0.15.
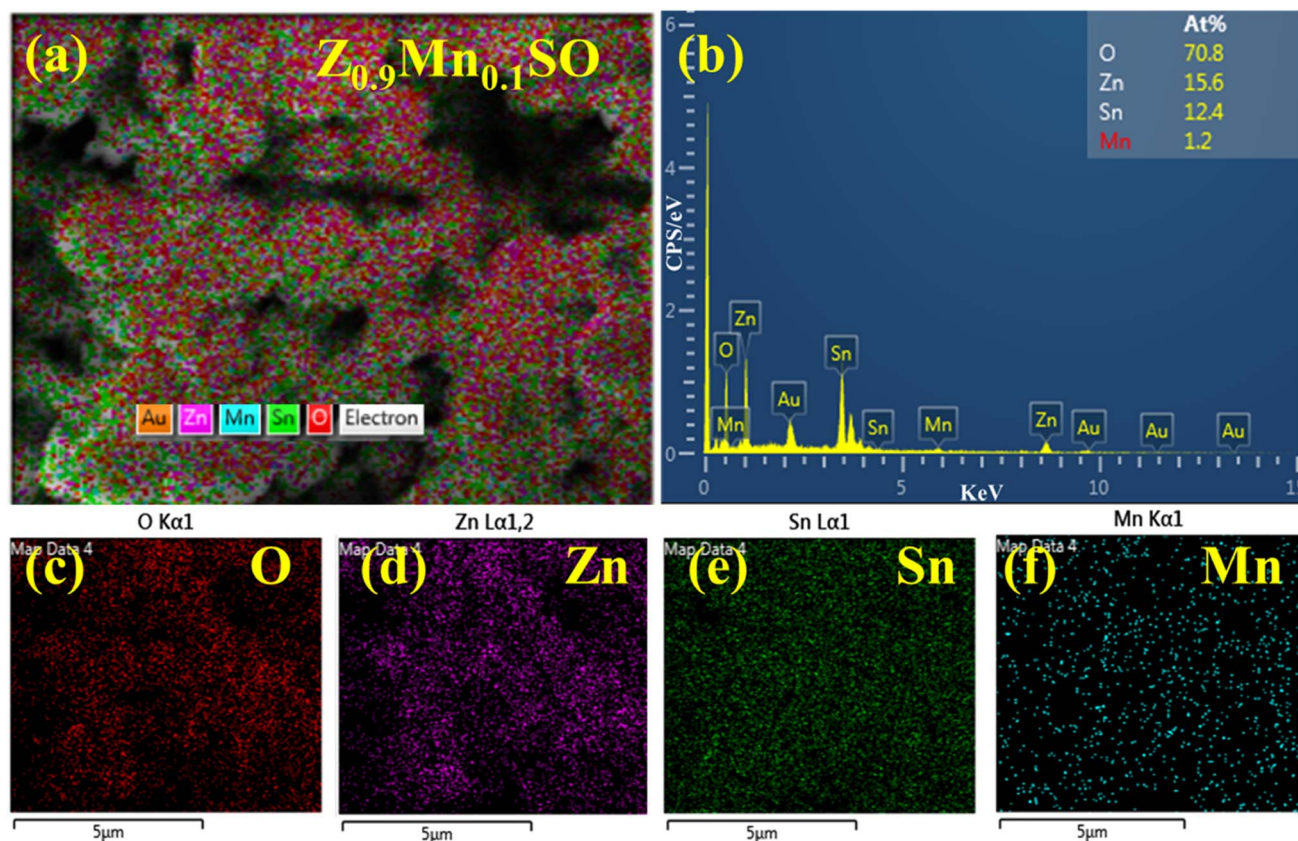
Fig. 5   (a–f) EDS spectrum and elemental mapping of $Zn_{1-x}Mn_xSnO_3$ samples, $x = 0.1$.

ZnSnO$_3$ (ZSO) and Z$_{0.9}$Mn$_{0.1}$SO samples. It indicates the existence of Zn, Sn, and O elements on the surface of ZSO samples and the presence of Zn, Sn, O, and Mn elements on the surface of Z$_{0.9}$Mn$_{0.1}$SO samples, which are consistent with the EDS observations. Fig. 7b presents the high-resolution spectra of Zn 2p, with two distinct peaks of Zn 2p in ZSO at binding energies of 1021.30 eV and 1044.24 eV signifying Zn 2p$_{3/2}$ and Zn 2p$_{1/2}$, respectively. However, the two distinct peaks of Zn 2p in Z$_{0.9}$Mn$_{0.1}$SO have an apparent shift to 1021.01 eV (Zn 2p$_{3/2}$) and 1044.09 eV (Zn 2p$_{1/2}$), respectively. Fig. 7c shows the high-resolution spectra of Sn 3d in ZSO and Z$_{0.9}$Mn$_{0.1}$SO. Two distinctive peaks of Sn 3d in ZSO are located at binding energies of 486.30 eV (Sn 3d$_{5/2}$) and 494.71 eV (Sn 3d$_{3/2}$), whereas the two distinctive peaks of Sn 3d in Z$_{0.9}$Mn$_{0.1}$SO are shifted to 485.84 eV (Sn 3d$_{5/2}$) and 494.26 eV (Sn 3d$_{3/2}$), respectively. The corresponding peaks of Zn 2p and Sn 3d demonstrate the existence of Zn^{2+} and Sn^{4+} in the samples. Deconvolution of the Mn 2p spectrum in Fig. 7d shows two distinct peaks at binding energies of 640.77 eV (Mn 2p$_{3/2}$) and 654.30 eV (Mn 2p$_{1/2}$) having orbital splitting energy of 13.5 eV, signifying the presence of Mn^{2+} in Z$_{0.9}$Mn$_{0.1}$SO samples. The apparent shift of the Zn 2p and Sn 3d characteristic peaks indicates the electronic interaction between the Mn^{2+} (dopant), Zn^{2+}, and Sn^{4+} sites. Mn-doping makes the sample electron rich due to the generation of vacancy defects. To analyze the impact of oxygen vacancy defects, O 1s peaks of ZSO and Z$_{0.9}$Mn$_{0.1}$SO have been analyzed,

as shown in Fig. 7e and f. The O 1s spectra are deconvoluted into three peaks: O$_L$ corresponding to lattice oxygen, O$_V$ caused by oxygen vacancy defect, and O$_C$ corresponding to chemisorbed oxygen. For the ZSO sample, the three peaks centered at 529.78 eV, 531.2 eV, and 532.79 eV are assigned to O$_L$, O$_V$, and O$_C$, respectively. Similarly, the three distinctive peaks of O 1s in the Z$_{0.9}$Mn$_{0.1}$SO sample are centered at 529.05 eV, 530.11 eV, and 531.46 eV, respectively. The relative percentages of each oxygen species are depicted in Fig. 7e and f, respectively. Compared with pure ZSO, there is a significant reduction in O$_L$ concentration for Z$_{0.9}$Mn$_{0.1}$SO (from 40.59% to 26.70%), whereas a surge in O$_V$ (from 38.52% to 45.25%) and O$_C$ (from 20.88% to 28.05%) concentrations, suggesting the beneficial use of Mn-doping for enhancing the gas-sensing performance of ZnSnO$_3$.

3.7   Gas sensing properties

The operating temperature plays an essential role in investigating the dynamic gas response of the sensor material. It significantly affects the adsorption–desorption phenomenon and reaction kinetics of the target gas with oxygen molecules on the sensor surface by improvising the activation energy in the sensing material.[33] Therefore, investigations were done to test the sensing performance of Zn$_{1-x}$Mn$_x$SnO$_3$ samples by exposing to 500 ppm CO gas at various altered operating temperatures of 50–300 °C. Fig. 8a–f depicted the n-type semiconducting
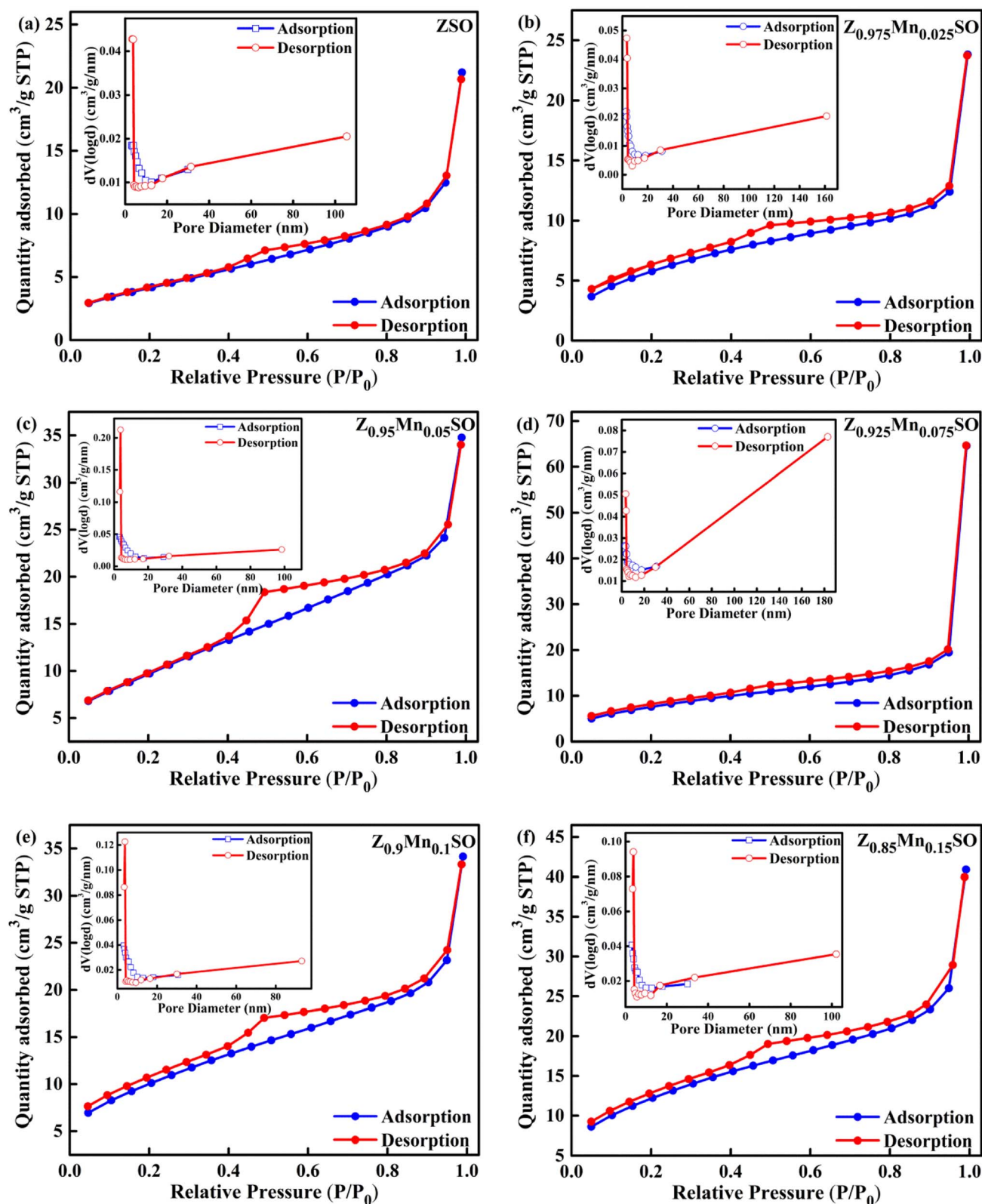
Fig. 6 N$_2$ adsorption−desorption isotherm and the corresponding BJH pore size distribution of Zn$_{1-x}$Mn$_x$SnO$_3$, $x=$ (a) 0, (b) 0.025, (c) 0.05, (d) 0.075, (e) 0.1, (f) 0.15.

behaviour of all these six materials because of the decrease in resistance with the increase in operating temperature. Initially, sensors were stabilized for a constant resistance value under exposure to fresh dry air at a particular operating temperature. When the sensors were exposed to CO (reducing gas), a decrease in electrical resistance value was observed, which gets stabilized

Table 2 Surface area, pore size, and pore volume of $Zn_{1-x}Mn_xSnO_3$ samples

Sample	BET ($m^2\,g^{-1}$)	Pore size (nm)	Pore volume ($cm^3\,g^{-1}$)
ZSO	15.229	3.097	0.03279
$Z_{0.975}Mn_{0.025}SO$	21.340	3.088	0.03692
$Z_{0.95}Mn_{0.05}SO$	27.878	3.075	0.05281
$Z_{0.925}Mn_{0.075}SO$	30.261	3.060	0.05379
$Z_{0.9}Mn_{0.1}SO$	36.294	3.099	0.09990
$Z_{0.85}Mn_{0.15}SO$	42.999	3.091	0.06328

for a while and returned to the initial value after the CO supply was cut-off and re-exposed to the fresh dry air. It is obvious from Fig. 8 that Mn-doped ZSO sensors exhibit more decline in resistance value than that of pure ZSO sensors and thus exhibit higher response.

As shown in Fig. 9a and b, the maximum percentage change in the resistance of sensors at different operating temperatures from 50 °C to 300 °C towards 500 ppm CO was calculated and represented in terms of the response by using eqn (1). The sensing response of all the sensors was seen to follow "increase-maximum-decrease" tendency.[15] Fig. 9 shows that for the pure ZSO sensor, there is a small change in response, and the maximum response is 5.79% at the operating temperature of 250 °C. However, for the entire Mn-doped ZSO sensor, the operating temperature significantly drops down to 200 °C with the remarkable enhancement in respective responses. As shown in Fig. 9a, ZSO sample doped with 10 at% Mn achieved the best

response of ∼311.37% at the 200 °C operating temperature. Because $Z_{0.9}Mn_{0.1}SO$ sample displays the best gas response to CO, the optimized value of Mn-doping is 0.1 (10 at%). As a result, the $Z_{0.9}Mn_{0.1}SO$ sample was chosen as a propitious candidate for further studies in our work.

The response time and recovery time are other essential parameters to judge the new generation gas sensor for fast detection of particular gases and speedy recovery to its ambient conditions in real application fields. The response and recovery time of the 0%, 2.5%, 5%, 7.5%, 10%, and 15% Mn-doped ZSO sensors towards 500 ppm CO at 200 °C were measured (shown in Fig. S3†) for the 90% of resistance changes and the compared results are as shown in Fig. 9c. Here, it is clearly observed that the $Z_{0.9}Mn_{0.1}SO$ sensor exhibits the shortest response time of 6.6 s among all the six samples and also the accelerated desorption rate of CO on $Z_{0.9}Mn_{0.1}SO$ due to the presence of Mn with the recovery time of 34.1 s.

Selectivity is another critical parameter to define the gas sensor's ability to differentiate a specific target gas from other interfering gases. The responses (%) of the $Z_{0.9}Mn_{0.1}SO$ sample towards exposure to four different gases, carbon monoxide (CO), ammonia (NH_3), ethanol (C_2H_5OH), and carbon dioxide (CO_2) were calculated at the operating temperature of 200 °C. As demonstrated in Fig. 9d, the $Z_{0.9}Mn_{0.1}SO$ sensor gives excellent responses to CO, whereas low responses to other interfering gases. Thus, the result from Fig. 9d inferred that the present $Z_{0.9}Mn_{0.1}SO$ sensor has excellent selectivity towards CO.

Fig. 10a presents the changes observed in resistance values of the $Z_{0.9}Mn_{0.1}SO$ sensor under the exposure of CO gas at
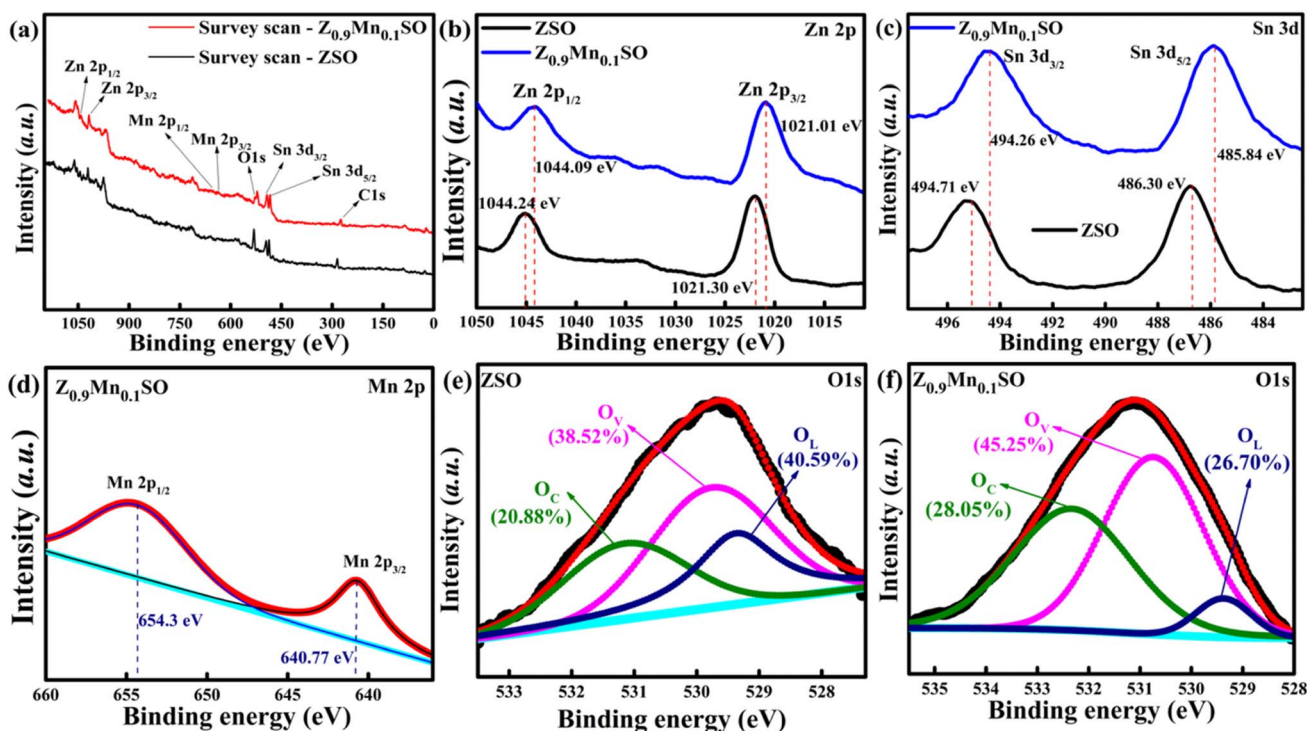

Fig. 7 The XPS spectra of ZSO and $Z_{0.9}Mn_{0.1}SO$ samples: (a) survey scan XPS spectra, (b) Zn 2p XPS spectra, (c) Sn 3d XPS spectra, (d) Mn 2p XPS spectra of $Z_{0.9}Mn_{0.1}SO$, (e) O 1s XPS spectra of ZSO, and (f) O 1s XPS spectra of $Z_{0.9}Mn_{0.1}SO$.
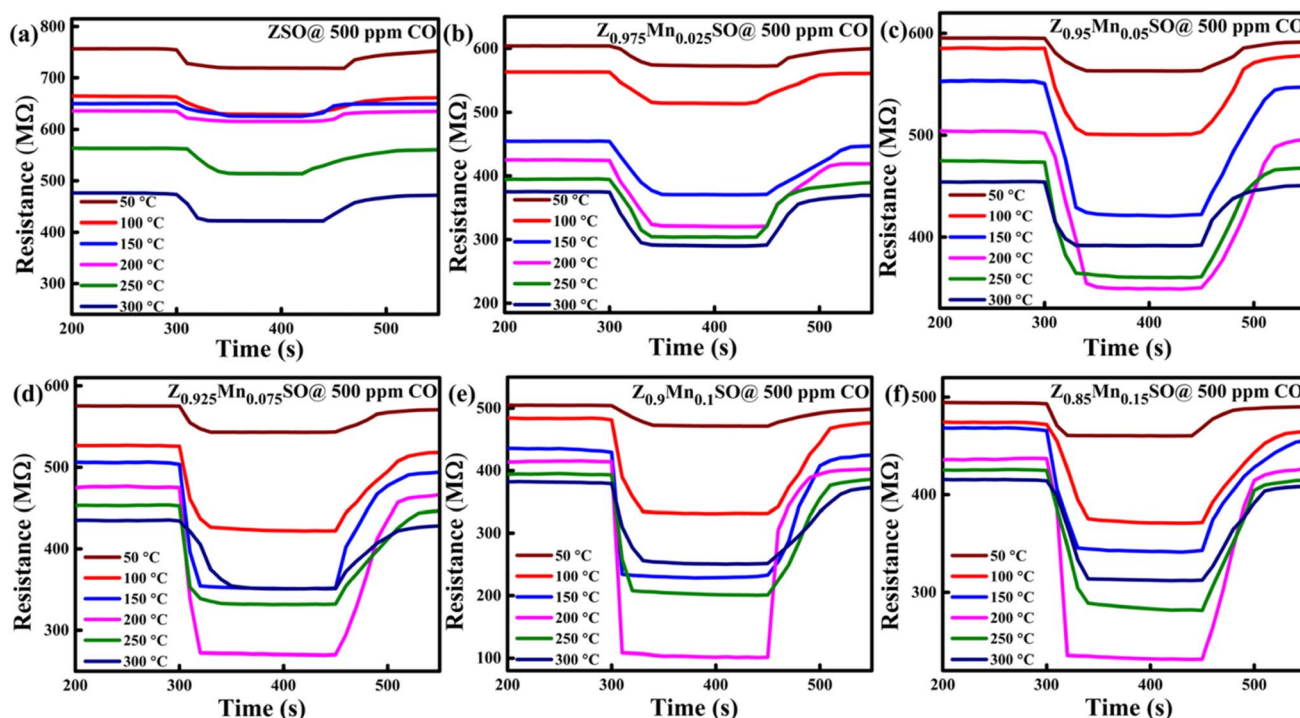
Fig. 8 Dynamic response–recovery curves of the gas sensor based on $Zn_{1-x}Mn_xSnO_3$, $x =$ (a) 0, (b) 0.025, (c) 0.05, (d) 0.075, (e) 0.1, and (f) 0.15.
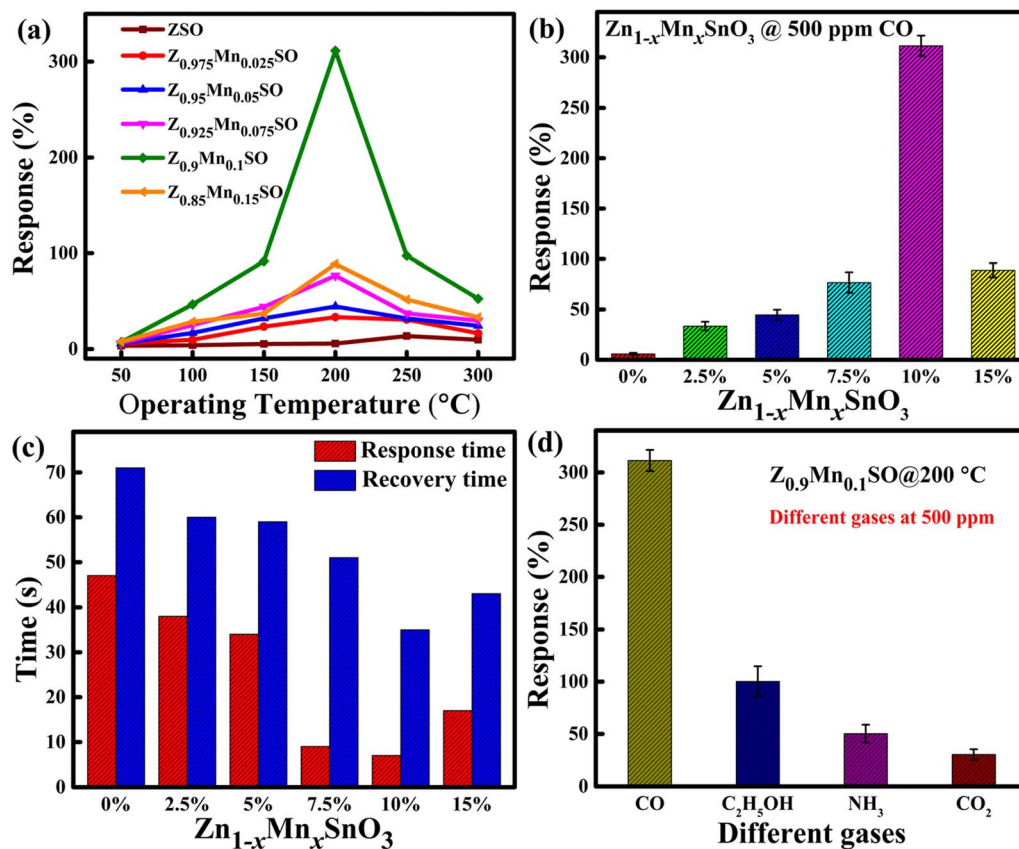

Fig. 9 (a and b) Relationship between the responses of gas sensor exposed to 500 ppm CO gas and operating temperature. (c) Comparison of the response and recovery times of $Zn_{1-x}Mn_xSnO_3$ sensors upon exposure to 500 ppm CO at the operating temperature of 200 °C. (d) Selectivity study by the comparison of $Z_{0.9}Mn_{0.1}SO$ sensor responses to different gases at the operating temperature of 200 °C.
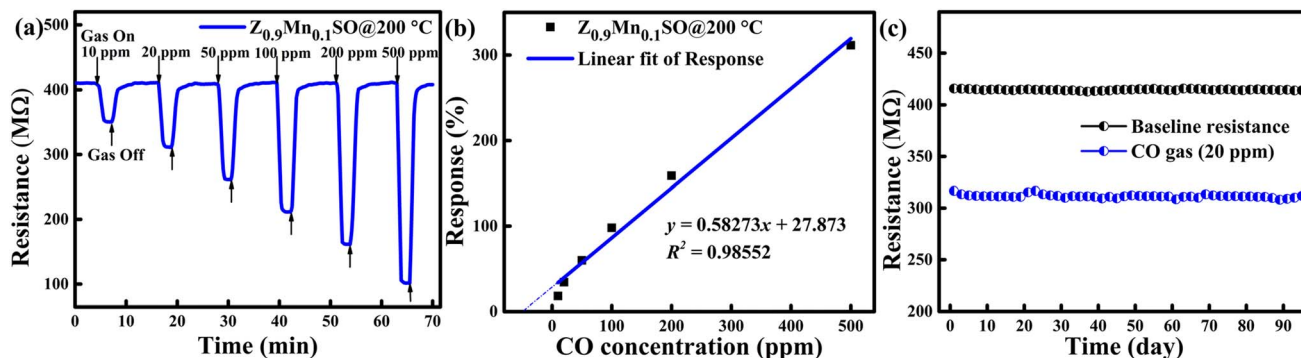
Fig. 10 (a) Dynamic response–recovery curves towards different varying CO gas concentrations; (b) calibration curve at 200 °C related to $Z_{0.9}Mn_{0.1}SO$ sensor. (c) Long-term stability test for the $Z_{0.9}Mn_{0.1}SO$ sensor responding to 20 ppm CO gas.

varying concentrations in the range of 10 to 500 ppm. It clearly represents the increase in resistance value with respect to the increase in CO concentration. Moreover, the rapid response as CO gas is injected, stable value in the presence of CO environment, and then sharp recovery to the initial value when the CO gas is removed were observed at all concentrations of CO gas. The percentage change in resistance was used to compute the responses (%) and Fig. 10b depicts the increased sensor response with CO concentration. An approximate good linear correlation was observed with the CO concentration, where the linear correlation value was found to be 0.98552. The good linear response to CO allows a lower detection limit in sub-ppm level, less than 1 ppm.

Long-term stability test of the $Z_{0.9}Mn_{0.1}SO$ sensor was also conducted over the period of 95 days at fixed 20 ppm CO and at the operating temperature of 200 °C as illustrated in Fig. 10c. It is clearly observed that the sensor shows no significant deviation in response, confirming the excellent long-term stability of the $Z_{0.9}Mn_{0.1}SO$ sensor.

Table 3 illustrates the comparison of the present work with the sensing performance of other MOS based CO sensors, basically based on binary type ZnO or SnO_2 or its ternary type compounds. It is worth noting that our sensor exhibited a comparatively high CO sensing performance, especially high response, low operating temperature, fast response, and recovery times.

3.8 Gas sensing mechanism

$ZnSnO_3$ belongs to the family of n-type metal oxide semiconductors whose gas sensing mechanism is exclusively based on the alteration in the electric resistance when exposed to the gas and explained by the most accepted oxygen adsorption–desorption theory on the material surface.[41] When $ZnSnO_3$ or $Zn_{1-x}Mn_xSnO_3$-based sensors are exposed to clean air, as shown in Fig. 11a and c, oxygen molecules present in the clean air will be adsorbed on the surface of the sensing material and captivate free electrons from the surface conduction band of the sensing layer. Depending on the operating temperature, adsorbed oxygen species reacting with free electrons transform into oxygen species of ionized form, such as O_2^-, O^-, O^{2-} (ref. 42) As a consequence, a thick electron depletion layer (EDL) will form, causing an increase in the electric resistance of the sensor, resulting in less flow of electrons inside the sensing material. Thus, the sensor material initially exhibits high resistance in the presence of clean air.
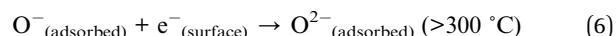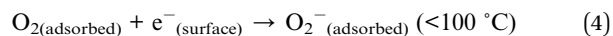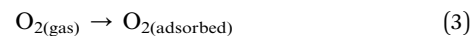
$$O_{2(gas)} \rightarrow O_{2(adsorbed)} \tag{3}$$

$$O_{2(adsorbed)} + e^-_{(surface)} \rightarrow O_2^-_{(adsorbed)} \ (<100 \ °C) \tag{4}$$

$$O_2^-_{(adsorbed)} + 2e^-_{(surface)} \rightarrow 2O^-_{(adsorbed)} \ (100–300 \ °C) \tag{5}$$

$$O^-_{(adsorbed)} + e^-_{(surface)} \rightarrow O^{2-}_{(adsorbed)} \ (>300 \ °C) \tag{6}$$

Table 3 Comparison of recent metal oxide-based gas sensors for CO detection

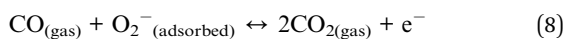| Sensing material	Operating temperature (°C)	CO (ppm)	Sensitivity (R_a/R_g) or response (%)	Response/recovery times (s)	Ref.
$ZnSnO_3$	250	500	5.79%	30/41	This work
$Zn_{0.9}Mn_{0.1}SnO_3$	200	500	311.37%	6.6/34.1	This work
SnO_2	310	200	7.29	16/28	34
SnO_2	200	91	84.3%	48/51	35
Ni^{2+}-doped SnO_2	350	1000	6.1	—	36
$TiO_{1.5}/ZnO$	300	48	1.365	166/343	37
$CuO-SnO_2$	200	100	3.52%	—	38
ZnO	250	100	3.7	—	39
$ZnO/ZnCo_2O_4$	300	10	17.3	60/50	40
Mn-ZnO	300	300	2.5	40/300	31
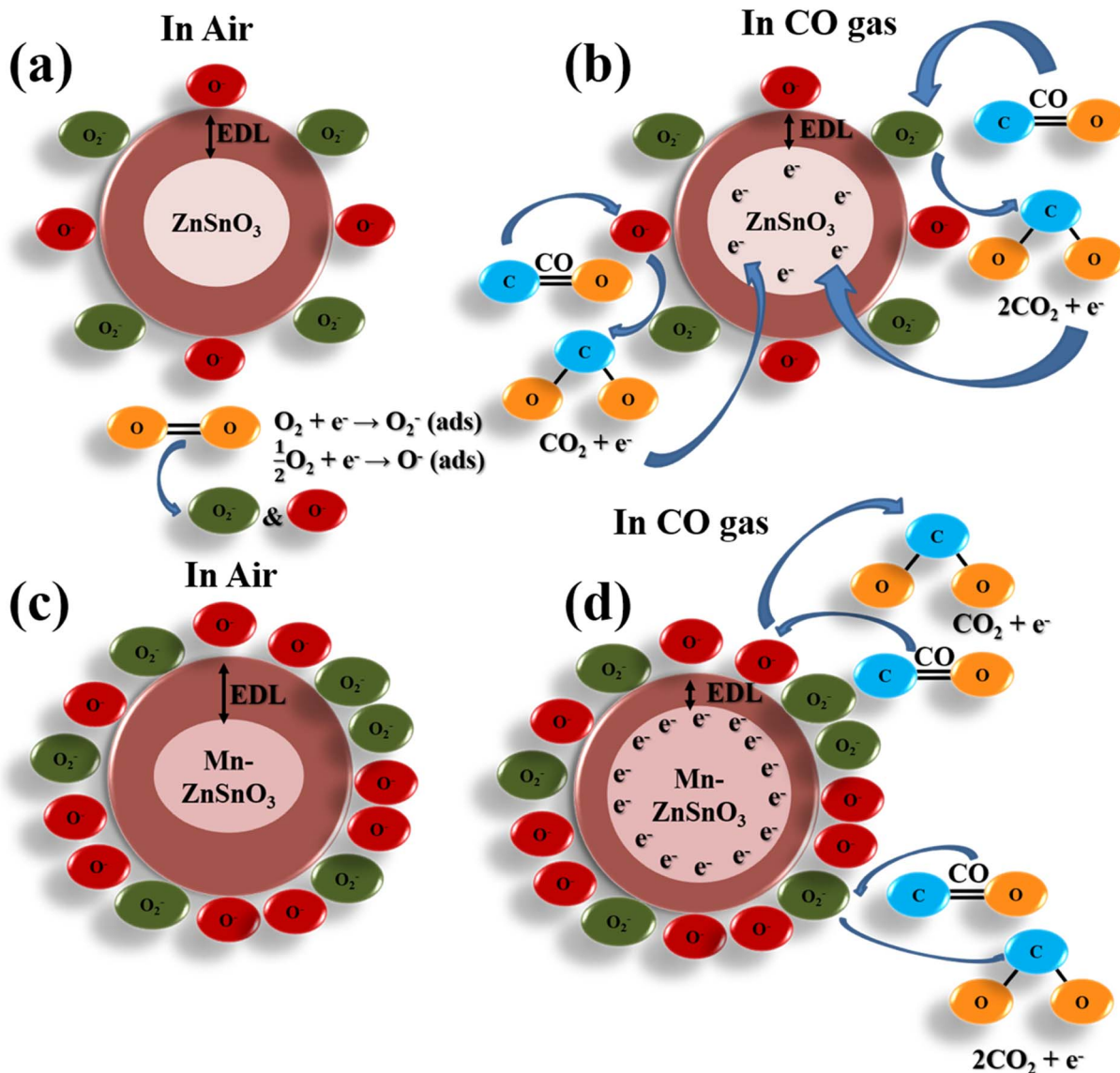
Fig. 11   The schematic diagrams for CO gas sensing mechanism of pure and Mn-doped $ZnSnO_3$ sensors in the presence of air (a) & (c) and in CO gas (b) & (d), respectively.

As shown in Fig. 11b and d, when the $ZnSnO_3$ sensor material is exposed to a reducing gas such as CO, the interaction between the CO gas and the predominant chemisorbed ionized oxygen species, O^-, can take place, and the electrons captivated by the chemisorbed O^- are released back into the conduction band of the sensing material, as per eqn (7), and produce CO_2. As a result, the thickness of the EDL layer is lessened and thus decreases the electric resistance of the sensing material, and the key redox reaction involved in the process of reaction with CO gas is as per the following equations:

$$CO_{(gas)} + O^-_{(adsorbed)} \leftrightarrow CO_{2(gas)} + e^- \tag{7}$$

$$CO_{(gas)} + O_2^-_{(adsorbed)} \leftrightarrow 2CO_{2(gas)} + e^- \tag{8}$$

Furthermore, as the gas sensing device is re-exposed to the clean air, oxygen molecules again react with the electrons captivated from the surface conduction band of the sensing material, which again forms the thick electron depletion layer, and thus, electric resistance recovers to the initial baseline.

In addition, the gas sensing performance of $ZnSnO_3$ is greatly related to the particle size, surface area, and metal oxidation states, which can be largely influenced by the doping of transition metal elements. Transition metals are most commonly used as sensitizers to enhance the gas sensing performance of sensing materials. The doping of $ZnSnO_3$ by the Mn element changes the particle size and increases the surface area, which results in alterations in the amount of adsorbed oxygen. It is well known that with the increase in the doping amount of Mn, the amount of oxygen molecules adsorbed increases for up to a certain concentration of Mn and then decreases.[43,44] For up to 10 at% Mn, maximum number of oxygen molecules transform into ionized O^- species and thus

more CO molecules are involved in the reaction process. Moreover, an extra thick electron depletion layer may form at the interface with the increase in Mn concentration. Thus, when the Mn-doped $ZnSnO_3$ sensors are exposed to the CO environment, a large number of electrons are freed and released back into the conduction band of the sensing material, $ZnSnO_3$ microspheres, more conveniently. Also evidenced from the XPS spectra, doping with Mn generates more oxygen vacancies in the ZSO lattice and hence more free electrons, improving the gas sensing. Simultaneously, the Mn site in $ZnSnO_3$ plays a critical role in adsorbing CO molecules at all temperatures. CO molecules are preferably adsorbed on the Mn sites to form bonds between Mn and CO. The interaction results in the donation of 5σ electrons of CO to the metal and π electrons back bonding from d-orbitals of Mn to CO. First, the CO molecules adsorb at the Mn sites and then migrate from Mn sites to Zn sites, through which Mn sites improve the CO adsorption and their interaction with oxygen species. Therefore, the doping of transition metal Mn effectively helps in intensifying the gas sensing performance of $ZnSnO_3$ microspheres towards CO gas.

4 Conclusions

In summary, porous Mn-doped $ZnSnO_3$ microspheres were synthesized by a simple co-precipitation method. The characterization results revealed that the Mn-doped $ZnSnO_3$ maintains the face-centered cubic structure of pure $ZnSnO_3$ and exhibits micro spherical morphology in the increasing order of surface area with the Mn concentration. The Mn-doping was confirmed by XPS. The BET measurements revealed an increase in surface area with an increase in Mn doping. The gas sensing performance analysis of $Zn_{1-x}Mn_xSnO_3$ chemi-resistive sensors with different Mn concentrations towards CO gas displayed enhanced sensing characteristics with respect to pure $ZnSnO_3$ sensors. To be specific, the MOS sensor based on 10 at% Mn-doped $ZnSnO_3$ exhibited a remarkably high response to CO gas at the reduced operating temperature of 200 °C. Moreover, the $Z_{0.9}Mn_{0.1}SO$ sensor exhibit fast response and recovery times of 6.6 s and 34.1 s, respectively, with good stability and reproducibility. The enhanced gas sensing properties with respect to CO can be ascribed to the sensitization effects of Mn and porous structure. On the basis of this study, these Mn-doped porous $ZnSnO_3$ microspheres are propitious to be applied for practical applications for monitoring CO gas in air.

Author contributions

Manish Kumar Tiwari: formal analysis, conceptualization, methodology, investigation, validation, visualizations, writing – original draft, writing – review and editing. Subhash Chand Yadav: formal analysis, visualizations, validation, writing – review, and editing. Abhishek Srivastava: writing – review and editing. Archana Kanwade: writing – review and editing. Jena Akash Kumar Satrughna: writing – review and editing. Sawanta S. Mali, Jyoti V. Patil and Chang Kook Hong: resources, writing – review and editing. Parasharam M. Shirage: formal analysis,

methodology, resources, validation, writing – review and editing, supervision, project administration.

Conflicts of interest

There are no conflicts of interest to declare.

References

1 C. Patel, B. Mandal, R. G. Jadhav, T. Ghosh, M. Dubey, A. K. Das, M. T. Htay, V. V. Atuchin and S. Mukherjee, *ACS Appl. Nano Mater.*, 2022, **5**, 2492–2500.

2 P. M. Shirage, A. K. Rana, Y. Kumar, S. Sen, S. G. Leonardi and G. Neri, *RSC Adv.*, 2016, **6**, 82733–82742.

3 W. Zhang, F. Yang, J. Xu, C. Gu and K. Zhou, *ACS Omega*, 2020, **5**, 20034–20041.

4 G. Shi, T. Yoon, S. Cha, S. Kim, M. Yousuf, N. Ahmed, D. Kim, H. W. Kang and K. S. Kim, *ACS Sens.*, 2018, **3**, 1102–1108.

5 A. Dey, *Mater. Sci. Eng., B*, 2018, **229**, 206–217.

6 A. K. Yadav, P. Rajput, O. Alshammari, M. Khan, Anita, G. Kumar, S. Kumar, P. M. Shirage, S. Biring and S. Sen, *J. Alloys Compd.*, 2017, **701**, 619–625.

7 S. Chand Yadav, A. Srivastava, V. Manjunath, A. Kanwade, R. S. Devan and P. M. Shirage, *Mater. Today Phys.*, 2022, **26**, 100731.

8 S. S. Nalimova, A. I. Maksimov, L. B. Matyushkin and V. A. Moshnikov, *Glass Phys. Chem.*, 2019, **45**, 251–260.

9 Q. Xie, Y. Ma, X. Zhang, H. Guo, A. Lu, L. Wang, G. Yue and D. L. Peng, *Electrochim. Acta*, 2014, **141**, 374–383.

10 S. C. Yadav, A. Sharma, R. S. Devan and P. M. Shirage, *Opt. Mater.*, 2022, **124**, 112066.

11 C. Fang, B. Geng, J. Liu and F. Zhan, *Chem. Commun.*, 2009, 2350–2352.

12 J. Xu, X. Jia, X. Lou and J. Shen, *Solid. State. Electron.*, 2006, **50**, 504–507.

13 Y. Yin, F. Li, N. Zhang, S. Ruan, H. Zhang and Y. Chen, *Inorg. Chem. Front.*, 2018, **5**, 2123–2131.

14 H. Men, P. Gao, B. Zhou, Y. Chen, C. Zhu, G. Xiao, L. Wang and M. Zhang, *Chem. Commun.*, 2010, **46**, 7581–7583.

15 G. Feng, Y. Che, C. Song, J. Xiao, X. Fan, S. Sun, G. Huang and Y. Ma, *Ceram. Int.*, 2021, **47**, 2471–2482.

16 L. Du, D. Wang, K. Gu and M. Zhang, *Inorg. Chem. Front.*, 2021, **8**, 787–795.

17 J. Zheng, H. Hou, H. Fu, L. Gao and H. Liu, *RSC Adv.*, 2021, **11**, 20268–20277.

18 B. S. Sá, C. A. Zito, T. M. Perfecto and D. P. Volanti, *Sens. Actuators, B*, 2021, **338**, 129869.

19 P. Wadkar, D. Bauskar and P. Patil, *Talanta*, 2013, **105**, 327–332.

20 X. Wang, J. Ma, Q. Ren, M. Wang, Z. Yang and J. Xin, *Sens. Actuators, B*, 2021, **344**, 130223.

21 X. Wang, T. Tao, Z. Qi, B. Leng, W. Xu, J. Ma and M. Wang, *Sens. Actuators, B*, 2021, **326**, 129013.

22 X. Wang, H. Li, X. Zhu, M. Xia, T. Tao, B. Leng and W. Xu, *Sens. Actuators, B*, 2019, **297**, 126745.

23 S. Bai, W. Tong, Y. Tian, H. Fu, Y. Zhao, X. Shu, R. Luo, D. Li and A. Chen, *J. Mater. Sci.*, 2019, **54**, 2025–2036.

24 I. Karaduman, M. A. Yıldırım, S. T. Yıldırım, A. Ateş, Y. A. Özdemir and S. Acar, *J. Mater. Sci.: Mater. Electron.*, 2017, **28**, 18154–18163.

25 E. Della Gaspera, M. Guglielmi, G. Perotto, S. Agnoli, G. Granozzi, M. L. Post and A. Martucci, *Sens. Actuators, B*, 2012, **161**, 675–683.

26 P. R. Chikate, A. Sharma, S. R. Rondiya, R. W. Cross, N. Y. Dzade, P. M. Shirage and R. S. Devan, *New J. Chem.*, 2021, **45**, 1404–1414.

27 A. Sharma, Y. Kumar and P. M. Shirage, *J. Mater. Sci.: Mater. Electron.*, 2018, **29**, 10769–10783.

28 R. Guo, Y. Guo, H. Duan, H. Li and H. Liu, *ACS Appl. Mater. Interfaces*, 2017, **9**, 8271–8279.

29 Y. Chen, B. Qu, L. Mei, D. Lei, L. Chen, Q. Li and T. Wang, *J. Mater. Chem.*, 2012, **22**, 25373–25379.

30 S. Paul, S. Basak and W. Ali, *ACS Omega*, 2019, **4**, 21827–21838.

31 M. H. Darvishnejad, A. Anaraki Firooz, J. Beheshtian and A. A. Khodadadi, *RSC Adv.*, 2016, **6**, 7838–7845.

32 H. Bai, H. Guo, C. Feng, J. Wang, B. Liu, Z. Xie, F. Guo, D. Chen, R. Zhang and Y. Zheng, *J. Mater. Chem. C*, 2022, **10**, 3756–3769.

33 Y. Fan, K. Li, X. Ren, W. Yan, C. Zhu, Y. Zhao, W. Zeng, Z. Chen and S. Wang, *J. Mater. Chem. C*, 2021, **9**, 17496–17503.

34 Q. Zhou, W. Chen, L. Xu, R. Kumar, Y. Gui, Z. Zhao, C. Tang and S. Zhu, *Ceram. Int.*, 2018, **44**, 4392–4399.

35 A. K. Gangwar, S. Srivastava, R. Godiwal, J. Jaiswal, P. Vashishtha, S. Pal, P. Pal, G. Gupta and P. Singh, *Opt. Mater.*, 2022, **128**, 112362.

36 L. S. Zhang and X. M. Guo, *Mater. Sci. Semicond. Process.*, 2022, **142**, 106516.

37 L. Vatandoust, A. Habibi, H. Naghshara and S. Mohammadi, *Surf. Interfaces*, 2022, **31**, 102001.

38 S. B. Dhage, V. L. Patil, P. S. Patil, J. Ryu, D. R. Patil and Y. S. Malghe, *Mater. Lett.*, 2021, **305**, 130831.

39 A. S. Mokrushin, Y. M. Gorban, N. P. Simonenko, E. P. Simonenko, V. G. Sevastyanov and N. T. Kuznetsov, *Russ. J. Inorg. Chem.*, 2021, **66**, 1447–1454.

40 Y. V. Kaneti, N. L. Wulan Septiani, I. Saptiama, X. Jiang, B. Yuliarto, M. J. A. Shiddiky, N. Fukumitsu, Y. M. Kang, D. Golberg and Y. Yamauchi, *J. Mater. Chem. A*, 2019, **7**, 3415–3425.

41 T. Zhou, T. Zhang, R. Zhang, Z. Lou, J. Deng and L. Wang, *ACS Appl. Mater. Interfaces*, 2017, **9**, 14525–14533.

42 X. Ma, S. Guo, J. Shen, Y. Chen, C. Chen, L. Sun, X. Zhang and S. Ruan, *RSC Adv.*, 2016, **6**, 70907–70912.

43 A. Xukeer, Z. Wu, Q. Sun, F. Zhong, M. Zhang, M. Long and H. Duan, *RSC Adv.*, 2020, **10**, 30428–30438.

44 Y. Bai, Y. Qin and P. Qiu, *Environ. Sci.: Nano*, 2021, **8**, 1096–1108.